Test-Retest Reproducibility of Reduced Field of View Density-Weighted CRT MRSI at 3T

Nicholas Farley *, Antonia Susjnar, Mark Chiew, Uzay E Emir *

Posted Date: 21 February 2024

doi: 10.20944/preprints202402.1211.v1

Keywords: Non-Cartesian; Nuclear; Magnetic; Resonance; Spectroscopy; Imaging; Test-Retest; Reproducibility

 doi:10.20944/preprints202402.1211.v1

Article

Test-Retest Reproducibility of Reduced Field of View Density-Weighted CRT MRSI at 3T

Nicholas Farley [1], Antonia Susjnar [2], Mark Chiew [3] and Uzay E Emir [1,2,*]

[1] School of Health Sciences, Purdue University, West Lafayette, Indiana, USA.; farleyn@purdue.edu (N.F.), uemir@purdue.edu (U.E.E.)
[2] Weldon School of Biomedical Engineering, Purdue University, West Lafayette, Indiana, USA.; asusnjar@mgh.harvard.edu (A.S.)
[3] Department of Medical Biophysics, University of Toronto, Toronto, Canada.; mark.chiew@utoronto.ca (M.C.)
* Correspondence: uemir@purdue.edu; Tel.: +17654941419

Abstract: Quantifying an imaging modality's ability to reproduce results is important for establishing its utility. In Magnetic Resonance Spectroscopic Imaging (MRSI), new acquisition protocols are regularly introduced, which improve upon their precursors with respect to signal-to-noise ratio (SNR), total acquisition duration, and nominal voxel resolution. This study has quantified the within-subject and between-subject reproducibility of one such new protocol (reduced-Field-of-View-Density-Weighted-Concentric-Ring-Trajectory (rFOV-DW-CRT) MRSI) by calculating the Coefficient of Variance of data acquired from a test-retest experiment. The Posterior Cingulate Cortex (PCC) and the Right Superior Corona Radiata (SCR) were selected as the Regions of Interest (ROIs) for Grey Matter (GM) and White Matter (WM), respectively. CVs for between-subject and within-subject are consistently around or below 15% for Glx, tCho, and Myo-Ins and below 5% for tNAA and tCr.

Keywords: non-cartesian; Nuclear; Magnetic; resonance; Spectroscopy; imaging; test-retest; reproducibility

1. Introduction

Non-invasive measurements of neurometabolites such as N-acetyl aspartate (NAA), a marker of neuronal loss/dysfunction, creatine (Cr), a marker for cell membrane turnover, glutamate (Glu), the primary excitatory neurotransmitter, and y-aminobutyric acid (GABA), the primary inhibitory neurotransmitter, are important for studying and diagnosing cranial diseases which lack an anatomical explanation. Proton Magnetic Resonance Spectroscopy (1H-MRS) is one of the physical means to non-invasively measure neurometabolic concentrations in vivo, making them essential for investigating neurological, neuropsychological, and oncological conditions [1]. Previous MRS studies have revealed significant differences in metabolic levels for cases of acute stroke, chronic multiple sclerosis, and brain tumors compared with a healthy brain [2]. Additional metabolites arise in specific conditions, such as succinate and acetate in abscesses, lipids in various abnormalities, propylene glycol after administration of parenteral preparations, or ethanol after alcohol consumption [2]. Since its conception, single-voxel-MRS (SV-MRS) has remained the preferred modality for quantifying neurometabolic concentrations, mostly for its fast acquisition and simple execution. However, the spectra are susceptible to partial-volume effects when different tissues (i.e., Grey Matter (GM), White Matter (WM), etc.) are within the measurement volume. Alternatively, multi-voxel-MRS (MRSI) can measure spectra from different regions at the same time, and with better resolution than SV-MRS, but requires longer acquisitions to compensate for its inherently lower signal-to-noise ratio (SNR).

Conventionally, MRSI acquisitions were cartesian because of their widespread use in standard Magnetic Resonance Imaging (MRI). Recently, many non-cartesian trajectories have been proposed and demonstrated to sample the spatial and spectral dimensions efficiently [3]. For example, the self-rewinding nature of concentric ring trajectories (CRTs) reduces the total acquisition duration by

 doi:10.20944/preprints202402.1211.v1

avoiding deadtimes associated with other trajectories [4,5]. It can be augmented to improve spectral bandwidth (SBW) by reconstructing interleaved trajectories produced via repeated measurements with different phase offsets. Theoretically, equidistant CRTs (e-CRTs) can fully sample k-space twice as fast as Echo-Planar Spectroscopic Imaging (EPSI) since an arbitrary number of rings (N) of e-CRTs can be substituted for a corresponding 2N rows of EPSI [1], but at the cost of poorly sampling the outer regions of k-space. More recently, it has been proposed to vary the distance between sampling radii according to a density-weighting (DW) formula, which may be tuned to improve outer k-space coverage in such a manner as to mimic a standard Hanning filter [6]. Nominal resolutions of 110 μL and 36 μL have been reported for 3D-MRSI using DW-CRTs at 3T, with an improvement to 20 μL achieved in 17 minutes at 7T [7], and for 2D-MRSI, a similar nominal resolution of 24 μL was obtained in 46 minutes at 9.4T [8]. Additionally, CRT Spatial-Spectral Encoding (SSE) has been observed to resist the appearance of aliasing (or "wrap-around") artifacts for situations where it would normally be expected, such as for EPSI when the field of view (FOV) is less than the size of the patient's head. In more recent work, a reduced FOV-^{1}H-MRSI (rFOV or ZOOM MRSI) sequence was proposed, which uses a combination of semi-adiabatic localization by adiabatic selective refocusing (semi-LASER), Metabolite Cycling, and DW-CRTs to measure localized metabolite signals without the appearance of aliasing artifacts [9]. Since the rFOV required fewer encoding steps (number of rings) to obtain higher resolutions, a higher nominal resolution and a faster acquisition time were achieved. The reported 2.5x2.5x10mm^3 (62.5 μL) resolution spectroscopic images were reconstructed using data acquired within 9.5 minutes at 3T [9]. To evaluate the reproducibility of this method, this study aims to determine the within-subject and between-subject reproducibility of the rFOV-DW-CRT-MRSI technique, as measured through a voxel-by-voxel Coefficient of Variance (CV) analysis on data acquired in the Posterior Cingulate Cortex (PCC) and Right Superior Corona Radiata (SCR) accomplished through a multi-session test-retest protocol.

2. Materials and Methods

2.1. Volunteers and Hardware

Data were acquired using a Siemens Prisma 3T MR system (Siemens, Germany) with a 64-channel head array receive coil and four volunteer subjects who did not present any neurological, neurodegenerative, or psychiatric disorders. Approval from Purdue's Institutional Review Board and written/informed consent from all subjects were obtained before the MR examinations.

2.2. Data Acquisition

T_1-weighted MPRAGE images were acquired for each subject with the following parameters: field of view (FOV)=240x240x176mm^3, TR=1900ms, TE=2.13ms, TI=900ms, flip angle=8, 176 transverse slices, 0.9x0.9x1mm^3 voxels. The rFOV-MRSI scan was planned on the T_1-weighted images to acquire data from the PCC and SCR, using the parameters described in Emir et al. [9], with rFOV = (120mm x 120mm x 10mm), in-plane matrix of 48x48 for a nominal voxel resolution of (2.5mm x 2.5mm x 10mm), semi-LASER localization, TR = 1500ms, and TE = 32ms. DW-CRTs were used for 2D-MRSI data sampling, with 64 points per ring, 24 rings, 4 interleaves, and a final spectral bandwidth (SBW) of 1.25kHz with 256 spectral points [9]. Instead of traditional water-suppression, metabolite cycling was used by applying either a standard or inverse excitation profile for non-water resonances. When done correctly, a water-suppressed spectrum can be calculated by subtracting the corresponding spectra [10]. Metabolite cycling reduces scan time by removing long pulse trains of water-suppression pulses [11]. The Volume of Interest (VOI) was centered on the posterior cingulate cortex. No angle was applied to the VOI versus the transverse plane. First and 2nd order B_0-shimming was performed through two iterations of Siemens' manual convergence method (GRESHIM) to optimize the coefficients for shimming coils in the VOI. A linewidth of less than 30Hz was obtained with this shimming protocol for all four subjects. After completion, the subject was removed from the scanner for 15 minutes before being sent back inside for a second set of identical scans.

 doi:10.20944/preprints202402.1211.v1

2.3. Data Processing

Spectroscopic k-space data were sampled via a non-cartesian DW-CRT SSE [6,10]. Raw files were exported offline for pre-processing, reconstruction, and quantification. The adjoint NUFFT (Non-Uniform Fast Fourier Transform) was used for reconstruction [6,12,13]. Metabolite quantification was performed using the LCModel package (Version 6.3-1M) as described in Emir et al. [9]. Only the 5 major neurometabolites were selected for further analysis by having Cramer-Rao Lower Bounds (CRLB) less than 15% for voxels within the relevant ROI. These were total Choline (tCho), total Creatine (tCr), combined Glutamate and Glutamine (Glx), Myo-Inositol (Myo-Ins), and combined NAA and NAA-glutamate (tNAA). LCModel results from each voxel were used to create metabolite maps for water-scaled quantification and tCr ratio. These metabolic maps were then co-registered with their corresponding T1-weighted MPRAGE image.

All co-registered metabolite maps and T_1-weighted MPRAGE images were converted into MNI-152 to facilitate voxel alignment between scans of different subjects. A direct comparison between MNI-152 and patient space metabolite maps can be seen in Figure 1. A shared coverage map for each subject was created by using one scan's tNAA metabolite map to mask that of the other. Masking refers to filtering out voxels correlated with values less than or equal to zero in another corresponding (masking) 2D image. Each subject's MNI-152 spatial overlap between their first and second spectroscopic imaging scans is shown in Figure 2. Subject 2's overlap is noticeably smaller than that of other subjects, which is why different masks were used for both scans to increase the number of voxels used in the statistical measurements. In contrast, the overlap of Subject 4 was noticeably greater than the others. A graphic depicting the overlap between a subject's cross-coverage map and the target ROI (GM and WM) is shown in Figure 3. The PCC was chosen as the basis for an ROI in GM. Its MNI-152 representation was made by taking every voxel from region 30 of the Harvard-Oxford Cortical Atlas and digitally masking them with the subject's shared-coverage mask. Likewise, the SCR was chosen as the basis for an ROI in WM, and its MNI-152 representation was made by taking every voxel from region 25 of the JHU ICBM-DTI-81 White-Matter Labels atlas and digitally masking them with the subject's shared-coverage mask.

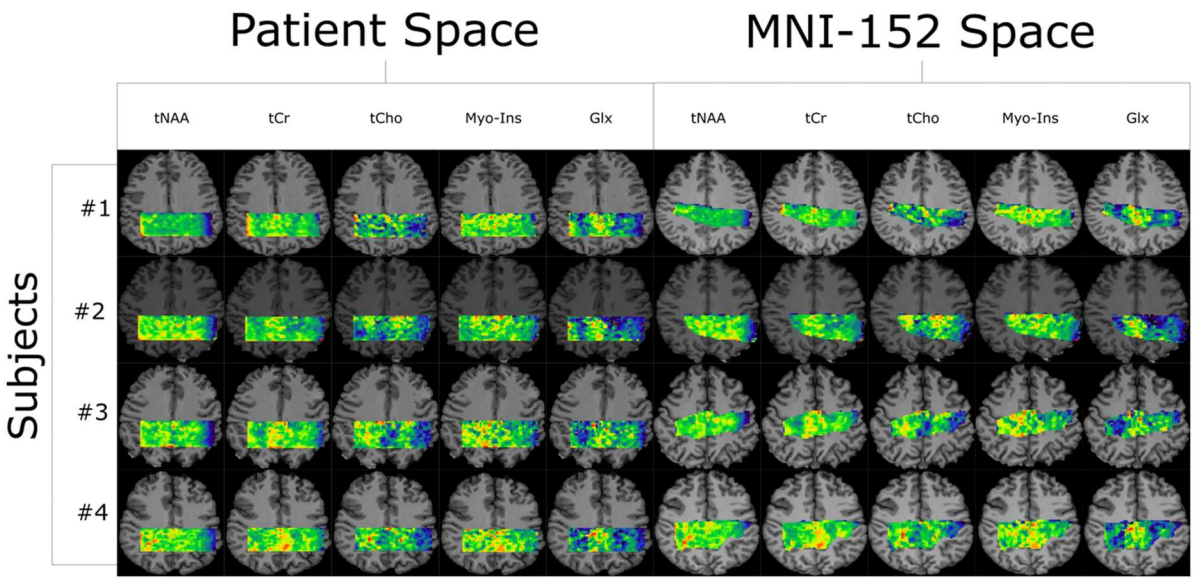

Figure 1. Quantification results from LCModel are plotted as five metabolite maps for each of the four subjects shown in both their native-patient space and as transformed into MNI-152.

 doi:10.20944/preprints202402.1211.v1

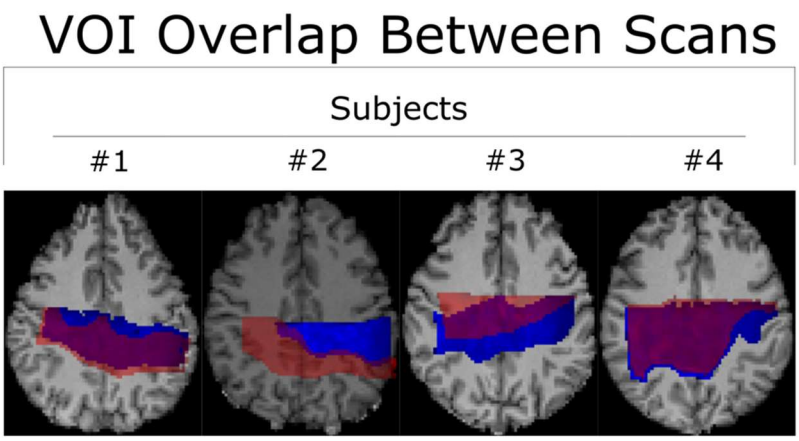

Figure 2. Two scans for each subject were acquired and then converted into MNI-152 space to facilitate direct comparison between voxels. The first and second scans are represented as blue and semi-transparent red, respectively.

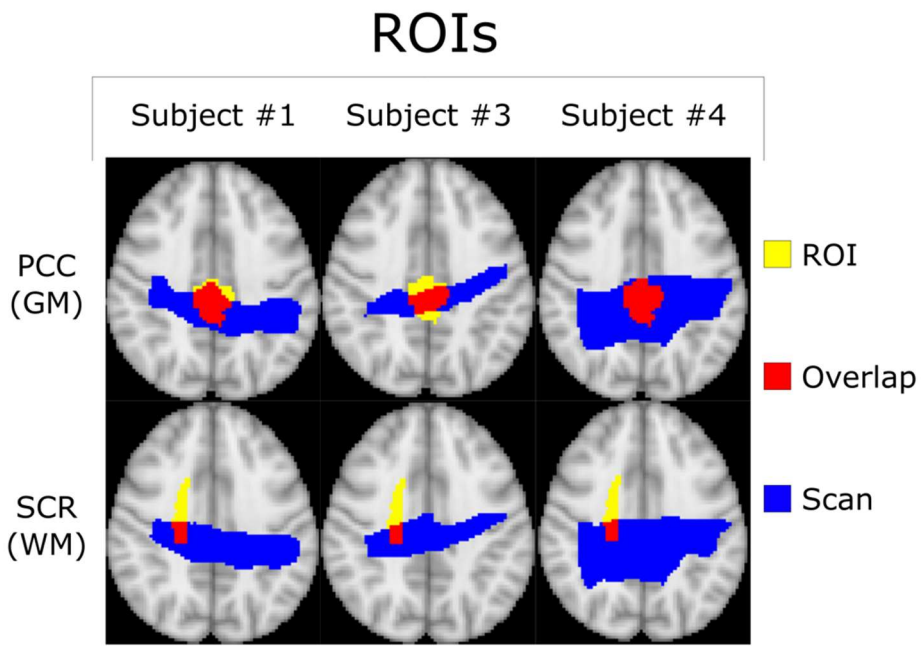

Figure 3. Transverse profiles of the standard MNI-152-2mm-Brain with the PCC and SCR ROIs defined by the Harvard-Oxford Cortical Atlas (GM) and the JHU ICBM-DTI-81 White-Matter Labels Atlas (WM). Voxels where the ROI and the subject's scan overlap are highlighted in red and included within the statistical analysis.

In addition to the water-reference and tCr-ratio MNI-152 metabolite maps mentioned, a separate set of Tissue-Weighted metabolic maps were generated by correcting the water-reference values for the tissue deviations in each voxel with the formula recommended in the LCModel manual [14,15]:

$$w_{conc} = \frac{43300 f_{GM} + 35880 f_{WM} + 55556 f_{CSF}}{1 - f_{CSF}}$$

Here, *f* is the partial volume fraction of a specific tissue type as denoted by its subscript. The partial volume fractions for each voxel were estimated using FSL's segmentation function (FAST) [16]

 doi:10.20944/preprints202402.1211.v1

to decompose each subject's MNI-152 T_1-weighted MPRAGE image into tissue-fraction maps (Number of input categories = 1, Number of classes = 3). With these parameters, the three maps correlate to GM, WM, and Cerebrospinal Fluid (CSF).

Furthermore, another separate set of metabolite maps was produced by normalizing the water-reference metabolite maps in each voxel by the total metabolic contribution:

$$\boldsymbol{n_i} = \frac{\boldsymbol{s_i}}{\sqrt{\sum_1^5 (\boldsymbol{s_i})^2}}$$

Here, n is the desired normalized metabolic concentration, s is the water-reference metabolic concentration, and the subscript i denotes one of the five major neurometabolites of interest (1:tCho, 2:tCr, 3:Glx, 4:Ins, 5:tNAA).

2.4. Statistical Analysis of Reproducibility

Both within-subject variance and between-subject variance for every combination of ROI, metabolite, and quantification ratio, were measured by the corresponding CV. This study defined CV as the ratio between the sample standard deviation and the mean. A sample consisted of subjects' first and second scans when measuring their specific within-subject CV. Metabolic concentration values for all voxels within an ROI were averaged together to calculate the ROI-specific metabolic concentration. Mean, standard deviation and CV were determined from ROI-averaged metabolic concentrations for every subject. The within-subject CVs from all subjects were then averaged to calculate the group within-subject Coefficient of Variance for both ROIs. For between-subject variance, it proceeded similarly but now with a sample combining the first scan from each subject.

3. Results

All subjects completed the acquisition protocol. Since the total number of overlapped voxels between Subject 2's scans was significantly lower than that of Subjects 1, 3, and 4, as may be seen in Figure 2, different regions of interest were used for each of the two scans to increase the sample size and improve statistical analysis.

3.1. Within-Subject and Between-Subject Reproducibility

The within-subject CVs for both ROIs are given in Table 1. LCModel determined the CRLB to be <5% for tNAA and tCr and <20% for tCho, Glx, and Myo-Ins for every voxel within the two ROIs for all four subjects. The CVs for tCho and Myo-Ins are consistently higher in GM than in WM. By contrast, Glx was noticeably higher in WM as opposed to GM. Furthermore, the within-subject CVs for tCr and tNAA are relatively identical for both ROIs. The between-subject CVs for all ROIs, metabolites, and quantification methods can also be found in Table 1. On average, the between-subject CV was greater than its corresponding within-subject CV. The relative differences between the average within-subject CVs and between-subject CVs are greater for metabolites contributing a larger portion of the total signal.

Table 1. Calculated Within-Subject and Between-Subject CVs for every combination of ROI, metabolite, and method used to report the data. Within-Subject CVs are on average less than their Between-Subject counterparts, with the greatest discrepancies occurring for tCr and tNAA.

 doi:10.20944/preprints202402.1211.v1

Table 1

Within Subject CV (%) Versus Method	Metabolites				
Grey Matter	tCho	tCr	Glx	Ins	tNAA
Absolute	11.0	1.8	10.0	12.1	2.0
Normalized	10.4	4.0	9.7	14.7	0.9
tCr Ratio	10.6	-	11.7	12.1	2.7
TF Correction	11.7	1.7	9.3	13.4	2.2
Average of Column	**10.9**	**2.5**	**10.2**	**13.1**	**2.0**
White Matter	tCho	tCr	Glx	Ins	tNAA
Absolute	8.5	4.2	16.1	8.8	1.9
Normalized	8.8	3.2	11.9	13.3	3.9
tCr Ratio	9.7	-	13.0	14.1	4.0
TF Correction	8.8	4.1	16.1	8.8	1.9
Average of Column	**9.0**	**3.8**	**14.3**	**11.3**	**2.9**
Between Subject CV (%) Versus Method	Metabolites				
Grey Matter	tCho	tCr	Glx	Ins	tNAA
Absolute	12.0	7.0	13.4	12.8	6.7
Normalized	10.7	3.7	8.3	13.4	3.7
tCr Ratio	11.3	-	10.2	12.4	4.0
TF Correction	12.5	7.2	12.5	14.4	7.6
Average of Column	**11.6**	**6.0**	**11.1**	**13.3**	**5.5**
White Matter	tCho	tCr	Glx	Ins	tNAA
Absolute	13.1	8.2	18.0	11.4	4.9
Normalized	10.7	3.4	15.3	12.6	5.2
tCr Ratio	10.2	-	16.9	13.1	6.3
PVE Correction	12.4	7.0	17.5	11.2	4.9
Average of Column	**11.6**	**6.2**	**16.9**	**12.1**	**5.3**

3. Discussion

This study performed a multi-session MRSI reproducibility experiment for rFOV-MRSI by acquiring two scans from four volunteers at 3T and then analyzing the statistical variance between and within subjects. The mean, standard deviation, and CV were calculated for each subject after using masks to select voxels corresponding only to the PCC or the SCR, which served as ROIs for GM and WM, respectively. These regions were selected for their predominantly homogeneous composition of their corresponding tissue type within the center and their heterogenous periphery. This study exploited the relatively high nominal resolution of the voxels to create irregular volumes that conform with the target ROI's shape and size. Emulating these irregular shapes for SVS-MRS and MRSI with >3mm resolution would be difficult, if not implausible, due to the structural variations occurring at <3mm scales.

Concentration maps with nominal voxel resolutions of 62.5 µL (2.5x2.5x10 mm^3) were produced using 2D-MRSI data in a clinically feasible acquisition time of 9.5 minutes on a Siemens 3T Prisma scanner. rFOV-DW-CRTs for sampling made this possible with its fast acquisition rate, intrinsically high-spectral resolution, and resistance to aliasing artifacts [9]. Despite the relatively small voxel volume and shorter acquisition duration, this study reports the within-subject CV for tNAA and tCr to be lower than what is reported elsewhere for SV-MRS reproducibility studies at 1.5T and 3T [17,18], and is comparable to MRSI reproducibility studies at 7T [13] at 3.1% and 2.9% for tNAA and tCr and 9.4T [19] at 5.6% for NAA/tCr.

The rFOV used in this study's MRSI sequence contributed to a more homogenous magnetic field within every voxel by reducing the spatial volume that the shimming algorithm needed to optimized. Furthermore, reducing the nominal voxel size reduced spectral linewidth, which can offset some of

 doi:10.20944/preprints202402.1211.v1

the sensitivity losses caused by the decreased signal-to-noise ratio from smaller voxels [20]. Even further, the removal of voxels through a digital mask improves magnetic field homogeneity and intra-voxel linewidth, which was only possible to reproduce across all subjects through MNI-152 space. Many previous test-reproducibility studies have relied on anatomical markers as the primary method to reproduce voxel placement across different scans, subjects, scanners, and medical centers [18,19,21–26]. While still used here, this study has additionally transformed all scanner data (anatomical and spectroscopic) into MNI-152 to facilitate alignment between voxels from different scans and subjects [25,26].

The relatively small spatial overlap between the first and second scans of Subject 2 after being transformed into MNI-152 space is likely due to the poor placement of the second scan's VOI in native-patient space. The sagittal viewing plane in Figure 4 shows that the location of the second scan (blue) is anatomically superior to that of the first scan (red) despite the nearly complete overlap along the transverse plane. The cause of this discrepancy was operator error at the time of the VOI's placement. Incidentally, this supports the notion that a non-operator-based method of aligning voxels (such as MNI-152) is necessary for quality control in reproducibility studies [27].

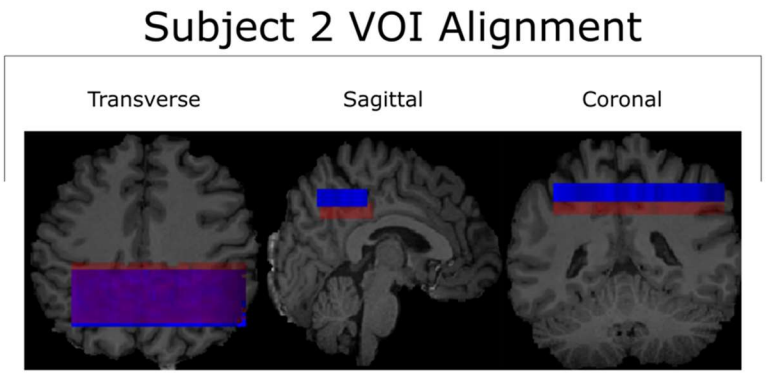

Figure 4. All three viewing angles for the VOI alignment of both scans for Subject 2. The misalignment between the two is visible along the sagittal and coronal planes. This misalignment is the greatest contributor to the small cross-coverage in the corresponding MNI-152 space as seen in Figure 2.

Calculated within-subject CVs suggest the variance is below the maximum threshold permitted to resolve actual variations in metabolic concentrations across scans. For example, the inverse relationship between the CVs for Glx and tCho (when comparing WM and GM) [18,19,21–24,28] can be seen from the data displayed in Table 1. Furthermore, Glx was found to have a higher variance in WM versus GM (16.1% vs. 10.0%) as opposed to tCho and Myo-Ins, where the opposite is seen to hold (8.5% vs. 11.0% and 8.8% vs. 12.1%, respectively). A higher level of variance is expected from metabolites with a lower total signal contribution, which is what other literature has reported for both grey and white matter [21,22,24]. Disease-related alterations to metabolite levels can be detected with 95% confidence if these alterations are greater than twice the Cramer-Rao Lower Bound [14]. Within-subject and between-subject CVs for all 5 major neurometabolites investigated were comparable with their average CRLBs calculated by LCModel. This suggests that low variations in metabolic concentrations are detectable. Since relevant pathology is known to cause alterations in metabolic concentrations, the alterations characteristic to different pathologies should also be detectable.

Calculated between-subject CVs are, on average, greater than their within-subject counterparts for all combinations of ROIs and metabolites. This is expected from any form of measurement that demonstrates a significant level of specificity and suggests the rFOV-DW-CRT's acquisition/reconstruction protocol can reliably differentiate between separate subjects.

 doi:10.20944/preprints202402.1211.v1

The difference between the average within-subject CVs and the average between-subject CVs are relatively larger for metabolites that contribute a greater fraction of the total signal {e.g., tCr (2.5% vs. 6.0% [GM] and 3.8% vs. 6.2% [WM]), and tNAA (2.0% vs 5.5% [GM] and 2.9% vs. 5.3 % [WM])}.

This study's acquisition protocol is constrained to only two dimensions, while 3D MRSI protocols have been proposed and documented previously in the literature [1]. If desired, the sequence can easily be converted into 3D through the addition of another phase encoding dimension or through the concept of Simultaneous Multi-Slice (SMS)-MRSI [29]. However, 2D-MRSI sequences, by restricting the size of the VOI, have an easier time shimming than their 3D counterparts since they only analyze a necessarily smaller segment of the brain, thereby allowing for our high resolution and relatively fast acquisition times.

4. Conclusion

A combination of rFOV-DW-CRT SSE, Metabolite Cycling for water suppression, and semi-laser localization have been simultaneously used to acquire in-plane nominal voxel resolutions of 2.5 x 2.5 mm^2 at 3T in a clinically feasible scan time of 9.5 minutes. Our study has quantified this protocol's within-subject and between-subject reproducibilities through their CVs and found them to be similar to what is reported for other MRSI modalities.

Author Contributions: Conceptualization, funding acquisition, methodology, investigation, data curation, formal analysis, and writing—original draft preparation, N.C, and U.E.E.; investigation, formal analysis, and writing—review and editing, A.S. and M.C. All authors have read and agreed to the published version of the manuscript.

Funding: This work was supported by grants to U.E.E. and N.F from the Wellcome Trust Collaborative Award (223131/Z/21/Z). This project was funded with support from the Indiana Clinical and Translational Sciences Institute, funded in part by Award Number UM1TR004402 from the National Institutes of Health, National Center for Advancing Translational Sciences, Clinical and Translational Sciences Award. The content is solely the responsibility of the authors and does not necessarily represent the official views of the National Institutes of Health.

Institutional Review Board Statement: The study was conducted in accordance with the guidelines of the institutional review board of Purdue University (protocol code 1102010525 on 24 January 2020).

Informed Consent Statement: Informed consent was obtained from all subjects involved in the study.
Data Availability Statement: All data, tables, and figures in this manuscript are original, and data are available upon request from the corresponding authors, as they have not been uploaded to an online database.

Conflicts of Interest: The authors declare no conflict of interest.

References

1. Moser, P.; Eckstein, K.; Hingerl, L.; Weber, M.; Motyka, S.; Strasser, B.; van der Kouwe, A.; Robinson, S.; Trattnig, S.; Bogner, W. Intra-Session and Inter-Subject Variability of 3D-FID-MRSI Using Single-Echo Volumetric EPI Navigators at 3T. *Magnetic Resonance in Medicine* **2020**, *83*, 1920–1929, doi:10.1002/mrm.28076.
2. Öz, G.; Alger, J.R.; Barker, P.B.; Bartha, R.; Bizzi, A.; Boesch, C.; Bolan, P.J.; Brindle, K.M.; Cudalbu, C.; Dinçer, A.; et al. Clinical Proton MR Spectroscopy in Central Nervous System Disorders. *Radiology* **2014**, *270*, 658–679, doi:10.1148/radiol.13130531.
3. Bogner, W.; Otazo, R.; Henning, A. Accelerated MR Spectroscopic Imaging—a Review of Current and Emerging Techniques. *NMR in Biomedicine* **2021**, *34*, e4314, doi:10.1002/nbm.4314.
4. Furuyama, J.K.; Wilson, N.E.; Thomas, M.A. Spectroscopic Imaging Using Concentrically Circular Echo-Planar Trajectories in Vivo. *Magnetic Resonance in Medicine* **2012**, *67*, 1515–1522, doi:10.1002/mrm.23184.
5. Jiang, W.; Lustig, M.; Larson, P.E.Z. Concentric Rings K-Space Trajectory for Hyperpolarized 13C MR Spectroscopic Imaging. *Magnetic Resonance in Medicine* **2016**, *75*, 19–31, doi:10.1002/mrm.25577.
6. Chiew, M.; Jiang, W.; Burns, B.; Larson, P.; Steel, A.; Jezzard, P.; Albert Thomas, M.; Emir, U.E. Density-Weighted Concentric Rings k-Space Trajectory for 1H Magnetic Resonance Spectroscopic Imaging at 7 T. *NMR in Biomedicine* **2018**, *31*, e3838, doi:10.1002/nbm.3838.
7. Hingerl, L.; Strasser, B.; Moser, P.; Hangel, G.; Motyka, S.; Heckova, E.; Gruber, S.; Trattnig, S.; Bogner, W. Clinical High-Resolution 3D-MR Spectroscopic Imaging of the Human Brain at 7 T. *Investigative Radiology* **2020**, *55*, 239, doi:10.1097/RLI.0000000000000626.

8. Nassirpour, S.; Chang, P.; Henning, A. High and Ultra-High Resolution Metabolite Mapping of the Human Brain Using 1H FID MRSI at 9.4T. *NeuroImage* **2018**, *168*, 211–221, doi:10.1016/j.neuroimage.2016.12.065.
9. Emir, U.E.; Sood, J.; Chiew, M.; Thomas, M.A.; Lane, S.P. High-Resolution Metabolic Mapping of the Cerebellum Using 2D Zoom Magnetic Resonance Spectroscopic Imaging. *Magnetic Resonance in Medicine* **2021**, *85*, 2349–2358, doi:10.1002/mrm.28614.
10. Emir, U.E.; Burns, B.; Chiew, M.; Jezzard, P.; Thomas, M.A. Non-Water-Suppressed Short-Echo-Time Magnetic Resonance Spectroscopic Imaging Using a Concentric Ring k-Space Trajectory. *NMR in Biomedicine* **2017**, *30*, e3714, doi:10.1002/nbm.3714.
11. Tkáč, I.; Deelchand, D.; Dreher, W.; Hetherington, H.; Kreis, R.; Kumaragamage, C.; Považan, M.; Spielman, D.M.; Strasser, B.; de Graaf, R.A. Water and Lipid Suppression Techniques for Advanced 1H MRS and MRSI of the Human Brain: Experts' Consensus Recommendations. *NMR in Biomedicine* **2021**, *34*, e4459, doi:10.1002/nbm.4459.
12. Nonuniform Fast Fourier Transforms Using Min-Max Interpolation | IEEE Journals & Magazine | IEEE Xplore Available online: https://ieeexplore.ieee.org/abstract/document/1166689 (accessed on 15 February 2024).
13. Fessler, J.A. On NUFFT-Based Gridding for Non-Cartesian MRI. *Journal of Magnetic Resonance* **2007**, *188*, 191–195, doi:10.1016/j.jmr.2007.06.012.
14. Provencher, S.W. Estimation of Metabolite Concentrations from Localized in Vivo Proton NMR Spectra. *Magnetic Resonance in Medicine* **1993**, *30*, 672–679, doi:10.1002/mrm.1910300604.
15. Provencher, S.W. Automatic Quantitation of Localized in Vivo 1H Spectra with LCModel. *NMR in Biomedicine* **2001**, *14*, 260–264, doi:10.1002/nbm.698.
16. Jenkinson, M.; Beckmann, C.F.; Behrens, T.E.J.; Woolrich, M.W.; Smith, S.M. FSL. *NeuroImage* **2012**, *62*, 782–790, doi:10.1016/j.neuroimage.2011.09.015.
17. Geurts, J.J.G.; Barkhof, F.; Castelijns, J.A.; Uitdehaag, B.M.J.; Polman, C.H.; Pouwels, P.J.W. Quantitative 1H-MRS of Healthy Human Cortex, Hippocampus, and Thalamus: Metabolite Concentrations, Quantification Precision, and Reproducibility. *Journal of Magnetic Resonance Imaging* **2004**, *20*, 366–371, doi:10.1002/jmri.20138.
18. Wijtenburg, S.A.; Gaston, F.E.; Spieker, E.A.; Korenic, S.A.; Kochunov, P.; Hong, L.E.; Rowland, L.M. Reproducibility of Phase Rotation STEAM at 3T: Focus on Glutathione. *Magnetic Resonance in Medicine* **2014**, *72*, 603–609, doi:10.1002/mrm.24959.
19. Ziegs, T.; Wright, A.M.; Henning, A. Test–Retest Reproducibility of Human Brain Multi-Slice 1H FID-MRSI Data at 9.4T after Optimization of Lipid Regularization, Macromolecular Model, and Spline Baseline Stiffness. *Magnetic Resonance in Medicine* **2023**, *89*, 11–28, doi:10.1002/mrm.29423.
20. Ebel, A.; Maudsley, A.A. Improved Spectral Quality for 3D MR Spectroscopic Imaging Using a High Spatial Resolution Acquisition Strategy. *Magnetic Resonance Imaging* **2003**, *21*, 113–120, doi:10.1016/S0730-725X(02)00645-8.
21. van de Bank, B.L.; Emir, U.E.; Boer, V.O.; van Asten, J.J.A.; Maas, M.C.; Wijnen, J.P.; Kan, H.E.; Oz, G.; Klomp, D.W.J.; Scheenen, T.W.J. Multi-Center Reproducibility of Neurochemical Profiles in the Human Brain at 7 T. *NMR in Biomedicine* **2015**, *28*, 306–316, doi:10.1002/nbm.3252.
22. Terpstra, M.; Cheong, I.; Lyu, T.; Deelchand, D.K.; Emir, U.E.; Bednařík, P.; Eberly, L.E.; Öz, G. Test-Retest Reproducibility of Neurochemical Profiles with Short-Echo, Single-Voxel MR Spectroscopy at 3T and 7T. *Magnetic Resonance in Medicine* **2016**, *76*, 1083–1091, doi:10.1002/mrm.26022.
23. Träber, F.; Block, W.; Freymann, N.; Gür, O.; Kucinski, T.; Hammen, T.; Ende, G.; Pilatus, U.; Hampel, H.; Schild, H.H.; et al. A Multicenter Reproducibility Study of Single-Voxel 1H-MRS of the Medial Temporal Lobe. *Eur Radiol* **2006**, *16*, 1096–1103, doi:10.1007/s00330-005-0108-y.
24. Wijnen, J.P.; van Asten, J.J.A.; Klomp, D.W.J.; Sjobakk, T.E.; Gribbestad, I.S.; Scheenen, T.W.J.; Heerschap, A. Short Echo Time 1H MRSI of the Human Brain at 3T with Adiabatic Slice-Selective Refocusing Pulses; Reproducibility and Variance in a Dual Center Setting. *Journal of Magnetic Resonance Imaging* **2010**, *31*, 61–70, doi:10.1002/jmri.21999.
25. Maudsley, A.A.; Domenig, C.; Sheriff, S. Reproducibility of Serial Whole-Brain MR Spectroscopic Imaging. *NMR in Biomedicine* **2010**, *23*, 251–256, doi:10.1002/nbm.1445.
26. Veenith, T.V.; Mada, M.; Carter, E.; Grossac, J.; Newcombe, V.; Outtrim, J.; Lupson, V.; Nallapareddy, S.; Williams, G.B.; Sheriff, S.; et al. Comparison of Inter Subject Variability and Reproducibility of Whole Brain Proton Spectroscopy. *PLOS ONE* **2014**, *9*, e115304, doi:10.1371/journal.pone.0115304.
27. Park, Y.W.; Deelchand, D.K.; Joers, J.M.; Hanna, B.; Berrington, A.; Gillen, J.S.; Kantarci, K.; Soher, B.J.; Barker, P.B.; Park, H.; et al. AutoVOI: Real-Time Automatic Prescription of Volume-of-Interest for Single Voxel Spectroscopy. *Magnetic Resonance in Medicine* **2018**, *80*, 1787–1798, doi:10.1002/mrm.27203.
28. Steel, A.; Chiew, M.; Jezzard, P.; Voets, N.L.; Plaha, P.; Thomas, M.A.; Stagg, C.J.; Emir, U.E. Metabolite-Cycled Density-Weighted Concentric Rings k-Space Trajectory (DW-CRT) Enables High-Resolution 1 H Magnetic Resonance Spectroscopic Imaging at 3-Tesla. *Sci Rep* **2018**, *8*, 7792, doi:10.1038/s41598-018-26096-y.

 doi:10.20944/preprints202402.1211.v1

29. Xia, P.; Chiew, M.; Zhou, X.; Thomas, A.; Dydak, U.; Emir, U.E. Density-Weighted Concentric Ring Trajectory Using Simultaneous Multi-Band Acceleration: 3D Metabolite-Cycled Magnetic Resonance Spectroscopy Imaging at 3 T 2019, 628594.